Extended x-ray-absorption fine-structure technique. II. Experimental practice and selected results

F. W. Lytle

The Boeing Company, Seattle, Washington 98124

D. E. Sayers* and E. A. Stern

Department of Physics, University of Washington, Seattle, Washington 98195
(Received 23 December 1974)

A technique is presented for obtaining extended x-ray-absorption fine structure (EXAFS) using a conventional, horizontal, x-ray diffractometer. Preparation of monochromator crystals, spectrometer alignment, counting techniques, evaluation of the energy scale and data normalization techniques are discussed. EXAFS spectra from a wide variety of materials are then presented to show the variability of the effect and interplay between various parameters of the theory. A final section illustrates a simple graphical scheme to obtain a first-neighbor distance from EXAFS data.

I. INTRODUCTION

This, and the following paper[1] (referred to as III), describe the experimental details and data-processing techniques which have been developed for examination of the extended x-ray-absorption fine structure (EXAFS). Both papers are cast in terms of a recent general theoretical paper by Stern,[2] referred to as I. In this technique the EXAFS is Fourier analyzed to produce a radial distribution function centered on the absorbing atom.[3] The particular utility of the technique is the ability to explore the environment of each atomic species in multicomponent noncrystalline materials such as amorphous semiconductors[4] or the highly dispersed materials used as catalysts.[5] The basic experimental determinant of the technique is a precise measurement with moderate resolution of the x-ray-absorption coefficient in the neighborhood of characteristic absorption edges. (For a general treatment of x-ray spectroscopy techniques, see Sandstrom.[6])

During an atomic x-ray-absorption event, an x ray with energy $h\nu$ disappears and a photoelectron of kinetic energy E is emitted from the atom conserving energy in the process

$$E = h\nu - E_K , \qquad (1)$$

where E_K is the initial binding energy of the electron. The absorption coefficient is identified as

$$\mu x = \ln(I_0/I) \text{ or } \ln(T/T_0) , \qquad (2)$$

where μ is the linear absorption coefficient, x is the absorber thickness, I_0 is the incident x-ray intensity, I is the transmitted intensity, and T and T_0 are the times to preset count with the absorber in and out of the beam. On the high-energy side of the absorption edge, μx shows fluctuations (EXAFS) which are related to the atomic arrangement immediately surrounding the absorbing atom. It was shown that the EXAFS $\chi(k)$ can be accounted for by a scattering model[7] formulated in I as

$$\chi(k) = \frac{m}{4\pi\hbar^2 k} \sum_j \frac{N_j}{R_j^2} t_j(2k) e^{-2R_j/\lambda} \sin[2kR_j + 2\delta_j(k)] e^{-2k^2\sigma_j^2} , \qquad (3)$$

where k is the electron wave vector, N_j is the number of atoms in the jth coordination sphere, R_j is the average radial distance to the jth atoms, $t_j(2k)$ is the back-scattering matrix element encountered by the electrons, λ is the mean free path of the electron, the 2nd exponential containing σ_j^2 is a Debye-Waller-type term where σ_j is the rms fluctuations of the atom about R_j, and $\delta_j(k)$ is a phase shift. The form of this equation is a sinelike scattering from each shell of atoms at R_j with the EXAFS signal proportional to the number of atoms surrounding the absorbing atom and inversely proportional to R_j^2. A decrease in temperature has the effect of sharpening the EXAFS. Each coordination sphere contributes a sinelike term of period $2kR_j$. The total result is a summation over all the coordination spheres within range of the effect.

Conceptually, EXAFS may be visualized as a kind of electron diffraction where the source of the electrons is within the material and originates from the atoms of that particular atomic species involved in the absorption event. The wave function of the excited photoelectron has an interference between its outgoing part and the diffracted part near the origin where overlap with the initial state occurs. This interference is either constructive or destructive depending on the wave number of the photoelectron, varying the dipole matrix element and thus the transition rate, producing the EXAFS variations.
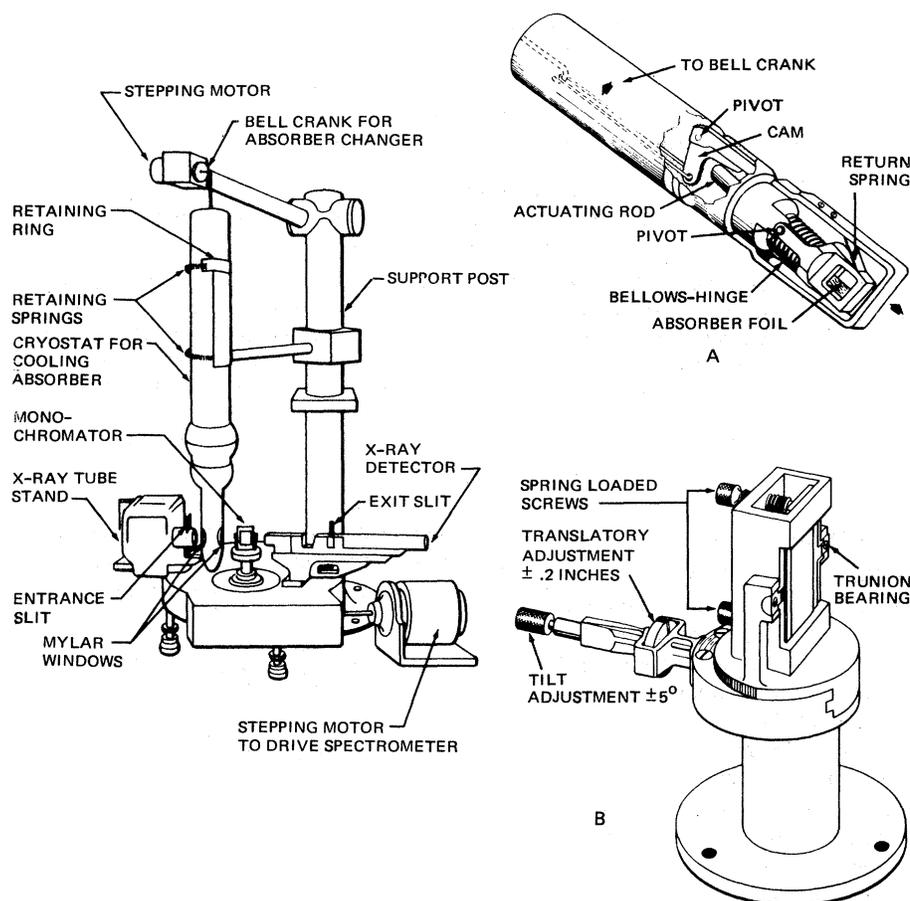
FIG. 1. Sketch of EXAFS apparatus showing the horizontal spectrometer, cryostat, and supporting post. (a) Sample holder and movement mechanism. Rotation of the stepping motor bell crank to which the pull-rod is attached, lifts the pull-rod which pushes the cam against the actuating rod, and displaces the sample holder to one side using the bellows as a hinge. Return spring moves the holder back when the pull-rod is released. There is also a stiffer spring at the top of the pull-rod to provide override relief. (b) Monochromator support allows translation in the plane of the spectrometer in a direction perpendicular to the incident x-ray beam, a tilt adjustment about the crystal center, as well as the θ adjust motion of the original spectrometer.

II. EXPERIMENTAL APPARATUS

A. X-ray spectrometer

Our basic x-ray spectrometer shown in Fig. 1 is a horizontal diffractometer with attached tube stand. The major modification is an improved crystal (monochromator) support for optimum alignment of the diffracting crystal [Fig. 1(b)]. This spectrometer is used with a conventional x-ray diffraction generator and tubes (Ag, W, or Mo target) chosen to provide a high-intensity continuum in the region of the absorption edge to be measured while missing the intense characteristic lines. The spectrometer is used with a goniometer radius of 18.75 cm using simple set-back brackets and an x-ray tube takeoff angle of approximately 3° (adjusted for maximum diffracted intensity).

The first slit is used to limit the angular divergence of the x-ray beam, and the Bragg-Brentano parafocusing conditions and slit position require the focusing (exit) slit to be approximately the same size. Between the two slits, a single-crystal monochromator Bragg diffracts a narrow band of the incident x-rays and adds its diffraction pattern to the divergence of the beam. The vertical divergence is limited to ± 2° by a Soller slit located before the exit slit. Thus the resolution function depends primarily on the size of the slits and the crystal diffraction pattern. (See Klug and Alexander[8] for a complete discussion of this type of spectrometer.) Our usual method of operation employs 0.05-mm slits (0.025° divergence) in the 2θ range from 15° to 45° and 0.1-mm (0.5° divergence) slits for angles greater than 45° with overlap as

experimentally required. Hence the resolving power defined as $(\tan\theta)/\Delta\theta$ (or $\lambda/\Delta\lambda$) is approximately 1000–2000. The diffracted intensity from the continuum operating at full recommended tube power is typically $(1-10)\times10^3$ photons per second before passing through the sample. For the case of 0.05-mm slits at $2\theta = 45°$ and a LiF crystal ($2d = 4.026$ Å), the energy-band width, assuming a rectangular response function, received at the exit slit would be ~ 4 eV ($\Delta E = E\cot\theta\Delta\theta$); however, the intensity distribution of the radiation filling the exit slit has the usual diffraction profile and the Rayleigh resolution criterion suggests that the spectrometer should be advanced in angular increments of $\frac{1}{2}$ the angular width of the exit slit, i.e., $\Delta 2\theta = 0.01°$ for 0.05-mm slits.

The mode of operation is as follows: For each spectrometer position, T and T_0 are measured (preset count mode) and stored on IBM cards, the spectrometer is advanced to the next 2θ position, and the sequence is repeated. A separate scaler is used to generate a running number for each subsequent pair (T, T_0). Knowledge of the start position and the 2θ stepping increment allows calculation of the x-ray wavelength for any data pair. The usual experiment involves 500–1000 data pairs. The spectrometer stepping motor and absorber changer are activated and synchronized by the x-ray scaler print-out command. It was found that the mechanical accuracy of the absorber placement mechanism limited the precision to $\sim 0.3\%$; thus 10^5 photons were recorded for each T, T_0, and increased precision to 0.1% was achieved by averaging multiple passes. The problem of coincidence loss in the x-ray detecting electronics was corrected using the method of Short[15] and Burbank.[16] If uncorrected, intense emission lines from the x-ray tube leave an image in the data, which can be mistaken for EXAFS.

The flanged tube stand attached to the spectrometer allowed the x-ray tube to be translated, rotated, and inclined with respect to the spectrometer circle. The alignment procedure consisted of locating (by means of these adjustments) the most intense spot on the x-ray tube target so that it was directed through narrow aligned entrance and exit slits at $2\theta = 0°$ as measured by a protected x-ray detector. The crystal monochromator was then inserted and a suitable characteristic line chosen for final crystal adjustment. At the calculated 2θ the translation, tilt and rotation (θ) adjustments of the crystal holder were used to obtain peak diffracted intensity of the standard line which located the diffracting volume of the crystal at the center of the spectrometer. Further refinement of the alignment was not necessary if the procedure described in the section on precision and accuracy of the energy scale was followed.

B. Monochromator crystals

The usual discussion of monochromators for x-ray spectrometers emphasizes high resolution with narrow crystal rocking curves and multicrystal spectrometers. Our requirement stresses high x-ray intensity at moderate resolution for good statistical accuracy of measured EXAFS. Although better resolution would probably show more detail, particularly near the edge, there is an inherent width (~ 20 eV) in the EXAFS due in part to temperature smearing as well as lifetime broadening,[9] e.g., 1.5 eV for the Cu K edge.

Given the flat crystal geometry, this experiment is intensity limited by the inherent luminosity of the x-ray tube and the diffraction efficiency of the monochromator. A given monochromator has a diffractive dispersion called its "rocking curve" which is the angular width of the diffracted beam. When the crystal is exposed to a continuum of diverging radiation, it selects from the total flux just that angular range of wavelength $\Delta\lambda$, which is its rocking curve width, and diffracts a narrow band toward the exit slit; thus a crystal with a very narrow rocking curve will diffract comparatively few photons. A crystal with a wider rocking curve than the divergence of the slit system will smear the diffracted beam over the exit slit. The optimum condition is obtained when the divergence of the slit system and the rocking curve of the monochromator are approximately equal.

The efficiency of diffraction and the rocking curve width of diffraction crystals may be modified by appropriate treatment. LiF(200) is a particularly workable crystal in this respect. The integrated reflection coefficient for nonpolarized radiation, which is the area under the crystal rocking curve, has been calculated as a function of wavelength for the two extremes of crystal perfection, a perfect crystal and an ideal mosaic crystal.[10,11] The measured values of selected cleaved and treated crystals are also shown.[11] Note that the treatment increased the photons diffracted by a factor of 3. The time necessary to obtain a precision measurement was reduced proportionately. The treatment consisted of vigorous sanding on rough paper to drive dislocations into the crystal followed by successively finer paper to 600 grit to provide a smooth surface. Part of the damaged surface layer was then removed by an etching procedure.[12] After 1 min in concentrated HF, a chemical polish consisting of 2-vol.% NH_4OH in H_2O at 26 °C with vigorous agitation was used to remove the surface at about 1 μm/min. The crystal was checked repeatedly until its rocking curve width narrowed to that of the desired slit size. We have used similar techniques with Si and quartz crystals with some success.

C. Cryostat and absorber preparation

EXAFS has been shown to be sensitive to temperature.[13] The degree of the effect at 77 and 295 °K is illustrated for Cu in Fig. 5. The Debye-Waller type exponential occurring in the theoretical expression for EXAFS can be related to an equation given by Shmidt,[14] which shows that for materials with a low value of characteristic temperature the effect will be largest; however, all materials will show an EXAFS intensity increase with lowering temperature, particularly, far from the absorption edge. For this reason, data were obtained routinely at 77 °K. It appears to be possible to use the temperature effect to directly evaluate the shell-to-shell coupling coefficients.[14] The difference in thermal vibration amplitude for the Cu data in Fig. 5 is evaluated in paper III.

The absorber samples were mounted in the 5-1 capacity glass cryostat shown in Figs. 1 and 1a. The design of the sample moving mechanism [Fig. 1(a)] accomplished its purpose without movable vacuum seals or introduction of a heat leak into the sample area. The x-ray transparent windows were Mylar epoxied to oval openings in the outer shell.

The absorber samples were prepared in a variety of ways: malleable metals were rolled (2–5 μm); some materials were evaporated onto Mylar or thin Al foil, soluble materials were dissolved and then absorbed and dried on filter paper, many materials were ground to pass 400 mesh, mixed with a suitable plastic glue (Duco) and solvent (acetone), and then cast on a smooth substrate. When dry, the casts were sandwiched between thin Al foil for support and thermal contact and attached to the sample holder. The optimum absorber thickness considering contrast, measurement time, and primarily the coincidence counting error problem, was attained when $I/I_0 \sim \frac{1}{3}$ on the high-absorption side of the edge. For experiments in which the element of interest was very dilute, thicknesses were used such that $I/I_0 \sim \frac{1}{10}$. For example, with this thickness a satisfactory L_{III} absorption pattern of 0.3-wt% Pt on Al_2O_3 was made in 15 passes.

D. Precision and accuracy of the energy scale

The kinetic energy of the ejected photoelectrons E must be established accurately in order to evaluate the natural EXAFS variable k. For every experiment, characteristic and/or impurity lines from the x-ray tube occurred and were used as standard reference points to calculate an effective lattice constant for the monochromator to establish the energy scale at the accuracy to which they were known.[17] Many elements were present as impurities on the x-ray tube anode; e.g., W, Cu, Pb, Ni, Ag, and Zn are usually present, plus the characteristic lines from the primary anode element in multiple

orders of diffraction. Replicate experiments established a precision of $\sigma = 75$ ppm (± 0.7 eV at the Cu K edge) as compared to 40 ppm for typical calibration lines. By using the calibration lines to calculate the lattice constant for every set of data, the requirement was removed for corrections involving the diffraction process in the monochromator crystal such as a temperature correction, Lorentz-polarization correction, refraction, and various errors due to misalignment. The value of E associated with each data pair was calculated from[18]

$$E = 12398.52/2d \, \sin\theta \, \text{eV}. \tag{4}$$

III. INITIAL DATA PROCESSING

The data collected from the EXAFS apparatus consisted of the time to collect a preset number of counts with the absorber in (T) and out (T_0) of the beam along with the corresponding angular position of the spectrometer. The preliminary data-processing program (i) tabulated the initial data and calculated the x-ray energy, the kinetic energy of the photoelectron, and the total absorption, (ii) removed the oscillatory part of the x-ray absorption from the smooth monotonic background, and (iii) normalized the data to a per-atom scale. These three program functions are described below. The total absorption was calculated at each point using Eq. (2), and the x-ray energy at each point was found from Eq. (4), where 2(d) was calculated as described previously, and θ at each spectrometer setting was found from the initial angle and fixed angular step. The kinetic energy E of the ejected photoelectron was then

$$h^2 k^2/2m = h\nu - E_K - E_0(k) = E - E_0(k) , \tag{5}$$

where k is the wave vector of the ejected photoelectron. E_K is the initial binding energy of the $1s$ electron which was ejected during the absorption of the x ray. The tabulated binding energies of Bearden and Burr were used,[17] which referenced the absorption edge to the Fermi energy; $E_0(k)$ is the inner potential and locates the point below the Fermi energy where the electron is, at least in principle, at rest. The treatment of $E_0(k)$ in the actual data analysis is discussed in III.

In the next step, the K-shell absorption contribution for the atomic species of interest was separated from all other absorption components, including other electrons in the same atom, absorption by other atoms in the sample, and absorption by the specimen support, which was usually Al foil. In the energy region of interest, these other components were far from any characteristic edges and could be adequately described by a Victoreen formula[19] of the form $\mu' = C\lambda^3 - D\lambda^4$, where λ is the x-ray wavelength and C and D were found by fitting

this formula to the measured absorption curve over an energy range (typically a few hundred eV) just below the K edge of interest. This fitted curve was then extrapolated to energies above the absorption edge to approximate all of the other absorption components and then subtracted from the experimental curve. The remainder was the K-shell contribution to the absorption including the EXAFS.

The removal of the oscillatory part of the x-ray absorption coefficient (EXAFS) from the smooth monotonically decreasing background absorption was a difficult problem, since neither calculated nor empirical curves existed which were accurate in the vicinity of the absorption edge. Rather than fitting some empirical function far above the edge and extrapolating back to the edge where large uncertainties may occur, we chose to use a Fourier filtering technique. This technique used a fast Fourier transform algorithm on the raw data (which was equispaced in θ) and takes 2048 data points and analyzes them in terms of the real and imaginary components of 1024 frequencies. Before the transform was taken, a straight line obtained from the first and last points of the data set was subtracted from the data set, which removed the sawtooth function which would occur in this kind of data because of the way in which the algorithm periodically continues the data. If left in, this sawtooth function would have considerable low-frequency components which could extend to frequencies comparable to the EXAFS frequencies. Some further reduction of the low-frequency components can be achieved by fitting and removing a parabola from the data.

The lowest frequency had a wavelength of twice the range of the data, and the remaining frequencies were the next 1023 harmonics of this fundamental. This spectrum has three components: (i) contributions at low frequencies due to the monotonically decreasing absorption coefficient, (ii) the EXAFS signal at intermediate frequencies, and (iii) small components from the random statistical counting noise uniformly distributed throughout the entire frequency range. The lowest EXAFS frequencies were estimated on the basis of the typical near-neighbor distances and were well separated from the low-frequency components which were then filtered by zeroing the first few low frequencies and retransforming the spectrum. This is shown in Fig. 2, where 70 of the first 1024 coefficients of a typical transform are shown. The remaining coefficients were negligible. The arrow indicates where a typical cut would be made to filter out the monotonic background. The retransformed spectrum contained only contributions from EXAFS and the high-frequency noise. If needed, the smooth absorption background could be found by subtracting this filtered spectrum from the raw data, as in Fig. 3(c). It may be more desirable to filter with a k

variable since θ space is nonlinearly related to k space and a sharp low frequency in θ space may be spread over a wide range of frequencies in k space.

The entire normalization procedure is illustrated in Fig. 3. Figure 3(a) shows the Ge K-edge EXAFS for amorphous GeSe along with the extrapolated Victoreen curve (dashed line) which was fitted to the data in the energy region below the edge. In Fig. 3(b), the EXAFS which was obtained from the data in Fig. 3(a) using the Fourier filtering technique is shown, and in Fig. 3(c) the smooth background curve obtained by subtracting the curve in Fig. 3(b) from the curve in Fig. 3(a) is also shown. Figure 3(c) also compares this smooth background curve $\mu_K^0(k)$ to both a Victoreen formula[19] and the empirical $\lambda^{2.73}$ curve suggested by McMaster.[20]

The final step in the initial data processing involved normalizing the data to the theoretical result derived in I:

$$\mu_K(k) = \mu_K^0(k)\left[1 + \chi(k) + \Delta\mu^s(k)\right] , \qquad (6)$$

where $\mu_K(k)$ is the total K-shell absorption coefficient, μ_K^0 is the absorption coefficient of the free atom, and $\Delta\mu^s$ is the correction to the absorption coefficient because the atoms are in a condensed
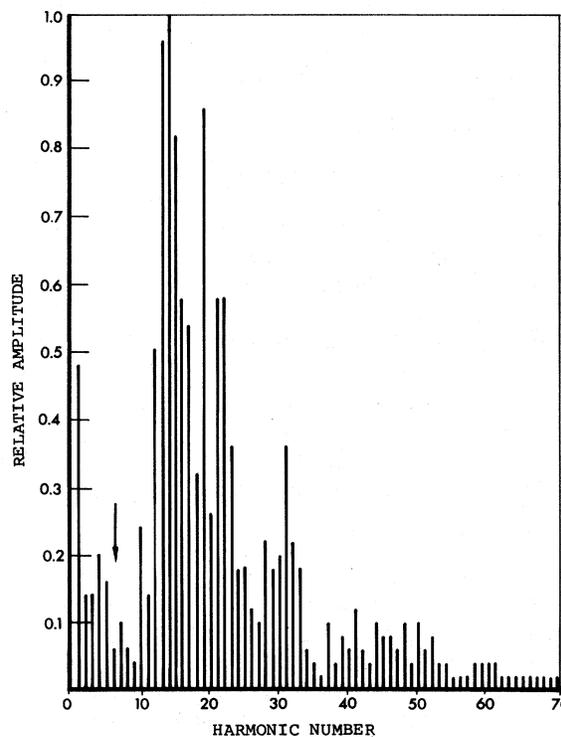
FIG. 2. Example of the frequency spectrum of raw data. Separation of EXAFS from the low-frequency slope components is apparent. Arrow indicates the low-frequency cutoff. Seventy of 1024 components are shown; higher components have very small amplitude.
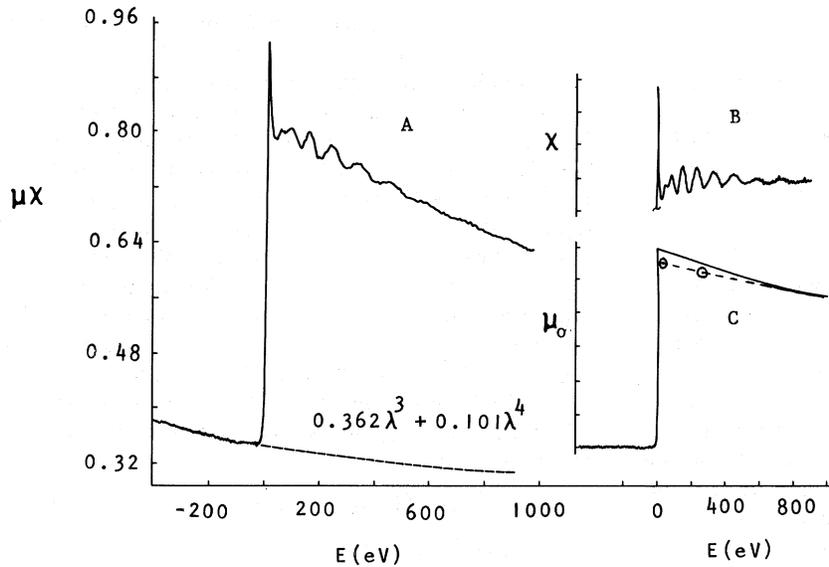
FIG. 3. (a) Measured K edge of Ge in amorphous GeSe where μx (absorption coefficient times thickness) is plotted vs photoelectron kinetic energy E. Dashed line is the Victoreen formula extrapolation due to absorption from other than the Ge K shell. (b) X vs E normalized and extracted from Fig. 6(a) as explained in the text. (c) Smooth K-shell absorption background $\mu_0(k)$ vs E which was used to normalize X according to Eq. (10). $\mu_0(k)$ is obtained from Fig. 6(a) by subtracting the Victoreen extrapolation and Fourier filtering to remove the EXAFS. Points, $\circ$ are extrapolations to the edge from a region 1000–1500 eV above the edge of a Victoreen form and the McMaster formula. Both are identical and approximately 5% below the measured curve.

state which modifies the atomic wave functions and is given by[2]

$$\Delta\mu^s = \tfrac{9}{16}\left[m^2 k^2/(2\pi^2 h^2)^2\right]\left[I_z(k)\right]^2 , \qquad (7)$$

where $I_z(k)$ is defined as

$$I_z(k) = \int \psi_k^+(\vec{r}') \, T(\vec{r}', \vec{r}'') \, \psi_k + (\vec{r}'') \, d^3r' \, d^3r'' \qquad (8)$$

and ψ_k^* is the initial outgoing photoelectron wave function, and T is the t matrix.

The EXAFS $\chi(k)$ is normalized to the same per-atom basis, which allows determination of absolute coordination numbers (as described in III), by rearranging Eq. (6),

$$\chi(k) = [1/\mu_K^0(k)] \, [\mu_K(k) - \mu^s(k)] , \qquad (9)$$

where the smooth absorption coefficient of the solid material $\mu^s(k)$ has been defined as

$$\mu^s(k) = \mu^0(k) + \Delta\mu^s , \qquad (10)$$

and is determined from Fig. 3(c). It is important to note that μ_K^0, which is the absorption coefficient of the free atom, will be different from μ_K^s, particularly at lower energies. This accounts for the enhancement of μ_K^s near the edge in Fig. 3(c) over the empirical formulas. This enhancement has been reported for several other materials by Del Grande,[21] who also includes atomic calculations by Scofield which in general fall on or below McMaster's curves. Parenthetically, we note that normalizing EXAFS in this way allows this mea-

surement of the difference in absorption between the solid and free-atom states, which may serve as a guide for future calculations.

To normalize the data according to Eq. (9), μ_K^0 must either be determined from empirical formulas or can be approximated by μ_K^s as determined in Fig. 3(c), which will give a small slowly varying error in the normalization. The normalized χ, E pairs are then used for Fourier analysis, as discussed in III.

We emphasize that this normalization procedure which divides out the λ^3 variation and subtracts the absorption due to all other materials (and other electrons in the same atom) is essential for evaluation of quantitative structural parameters, as discussed in III. However, if only interatomic distances are desired, Fourier inversion of any straightened-out EXAFS function will suffice, or the graphical technique discussed in Sec. II will allow determination of the nearest-neighbor distance.

IV. SELECTED DATA

In this section, a variety of normalized EXAFS data is plotted vs k [$k = (0.263E)^{1/2}$, neglecting E_0 and the errors involved which are discussed in III] to illustrate in a qualitative way the variables in the effect. In III, the data for Cu, Ge, and GeO_2 shown here are quantitatively analyzed to illustrate data-processing techniques. Van Nordstrand[22] has compiled absorption spectra in order to classify

coordination compounds in an empirical way. Lytle[23] compared the EXAFS of a few pure metals showing the effect of crystal structure; however, the spectra were not normalized and of less statistical accuracy than shown here. Because of problems connected with preparation of samples of uniform thickness a 0.1% precision was not always achieved in Figs. 4-8 but was at least 0.3%. With the exception of Fig. 4, all data were obtained at 77 °K, and all data were plotted to the same scale. The numerical scale in Fig. 4 is the same, but the graph is slightly enlarged in amplitude.

The effect of temperature (77 and 295 °K) is shown in Fig. 4 for Cu, which has a fairly low characteristic temperature (= 320); thus the effect is quite large. In III these data are analyzed to determine a quantitative measure of the first-shell thermal vibration. The effect of an increase in the first-shell coordination number is shown in Fig. 5, where from the top, hexagonal Se is 2-coordinated, diamond cubic Ge is 4-coordinated, body-centered-cubic Fe is 8-coordinated, and face-centered-cubic Ni is 12-coordinated. Since all of the data have been normalized and plotted to the same scale, the increase in EXAFS amplitude from top to bottom is real and shows the effect of and dominance by first-shell coordination number N_1 in the amplitude of EXAFS. Figure 5 also shows a large peak near the edge in Ge, the origin of which is presently not clear. It is of a character different from the rest of the EXAFS and is discussed in further detail in III. When Fourier analyzing the Ge data, the lower limit of the transform would be set so as to exclude this peak (as in III, Fig. 1),
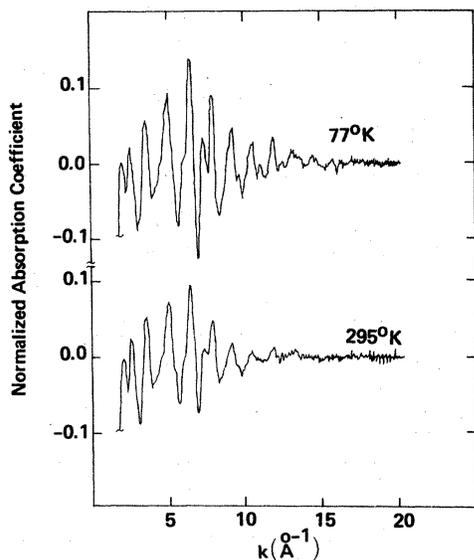
FIG. 5. EXAFS data for polycrystalline hexagonal Se, diamond cubic Ge, bcc Fe, and fcc Ni.

since it is not part of the EXAFS effect. Stern[2] has discussed the range of $k \geq 3$ over which the theory is expected to be valid.

In Fig. 6, the environment of each absorbing atom is tetrahedral; however, there is a wide range of character in the EXAFS. In particular, note the envelope of the EXAFS structure, as shown by the dotted lines for the Ge and GeO_2 spectra. This envelope is due to the $t_j(2k) e^{-2\sigma^2 k^2} e^{-2R_j/\lambda}$ terms and experimentally shows the following characteristics: (i) Metals and semiconductors such as Cu, Ge, or $GeSe_2$ show EXAFS beginning with low amplitude near the absorption edge (after possible band structure peaks, as in Ge) growing to a maximum near $k \approx 6-7$ and decaying exponentially after that. The effect of a temperature increase is to diminish the amplitude of all the EXAFS (but not the structure at the edge) with the expected $e^{-\sigma_j^2 k^2}$ dependence. (ii) Insulators, inorganic and organic compounds in general, do not show the build up and decay but begin with large amplitude at the edge with a rapid exponential decay, as in GeO_2 hexagonal and ZnS zinc blende. This effect may be characteristic of first-neighbor atoms of large size. When the EXAFS in Figs. 4-8 is Fourier transformed as in III, the various near-neighbor distances are clearly shown but with varying degrees of side-lobe structure due to the transform of the envelope function. Since this EXAFS envelope structure is sensitive to the kind of near neighbor as well as other physical parameters, it appears important to understand it and apply it to the characterization of materials. An empirical

FIG. 4. Effect of temperature on the EXAFS of 2.5-μm-thick, polycrystalline Cu.
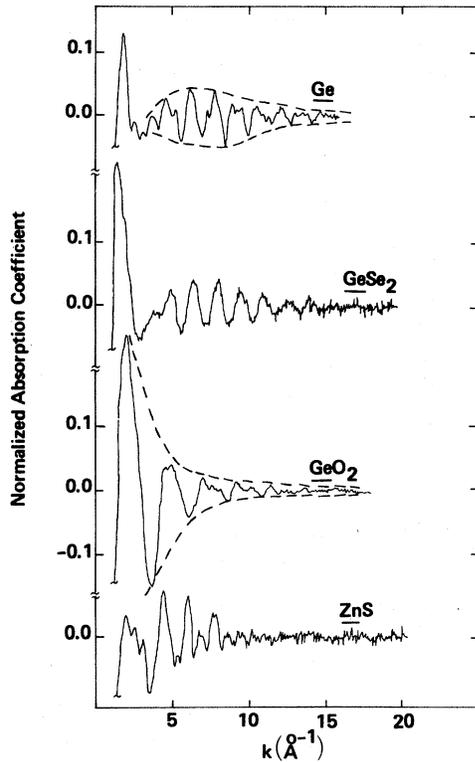
FIG. 6. EXAFS spectra for a group of 4-coordinated polycrystalline materials Ge, $GeSe_2$, hexagonal GeO_2, and zinc blende. In Figs. 6-8, the underlined element designates the K edge illustrated.

technique for isolating this function is shown in III.

Figure 6 also illustrates the small effect of large changes in the atomic number of the atoms in the first coordination sphere; i.e., O, S, Ge, and Se are present as the four first neighbors in GeO_2, ZnS, Ge, and $GeSe_2$, where the number of electrons present in the atom in the first coordination shell varies from 8, 16, 32, to 34, respectively. Note that the overall amplitude of the normalized EXAFS remains approximately the same, proving that the electron scattering term is not the usual electron form factor, contrary to what we expected in Ref. 3, but in agreement with Ref. 2. The amplitude of the EXAFS effect is most dependent upon the number of atoms in the first shell and not the total number of electrons on the atoms. Compare Se (2 neighbors, 68 electrons) in Fig. 5 with GeO_2 in Fig. 6 (4 neighbors, 32 electrons) or ZnS (4 neighbors, 64 electrons). Large electronegative atoms such as O^{2-}, Cl^-, F^- produce the characteristic EXAFS envelope with large amplitude excursions near the edge which decrease quickly; the Fourier transform of such materials resolves coordination peaks out to ~5 Å with a mean free path $\lambda \approx 3$ Å which is half that of metals and semiconductors.

The strongest EXAFS is present in metals (which also have the most tightly packed structures) and always shows the build up of the amplitude to a maximum near $k \approx 6-7$ with slow decay. Fourier transforms show peaks located at atomic positions out to ~10 Å and measured mean free path (as in III) $\lambda \approx 6$ Å. When the atoms in a coordination shell are spread over a range of distances as in Zn (Fig. 8), EXAFS is not as high in amplitude and has more detail.

In Fig. 7, the variability of EXAFS for the Co atom in a variety of materials is shown. Co metal is fcc with 12 nearest neighbors, CoO has the NaCl-type structure where Co has 6 oxygen neighbors. In $CoCl_2$, CoF_3, and $CoMoO_4$, Co has distorted octahedral coordination, and all show an exponential decay of EXAFS. The 4-wt% Co on Al_2O_3 (a catalyst) was found to be tetrahedrally coordinated. Note that the EXAFS for Co, Cu, and Ni (all fcc) is essentially identical except for scaling by the lattice parameter.

Figure 8 illustrates more examples of EXAFS. Compare Cr (bcc) with Fe in Fig. 5. Zn has a
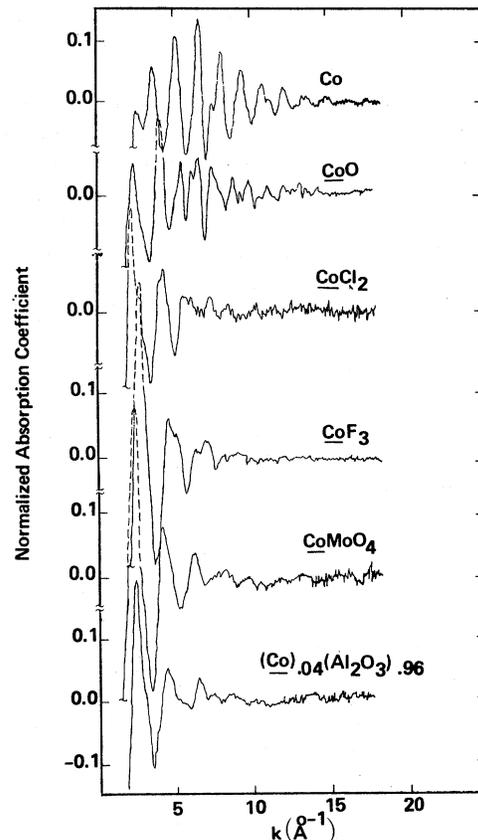
FIG. 7. EXAFS spectra for Co in a variety of polycrystalline materials. 4-wt% Co on Al_2O_3 was amorphous by x-ray diffraction with only very broad γ-Al_2O_3 diffraction lines present.
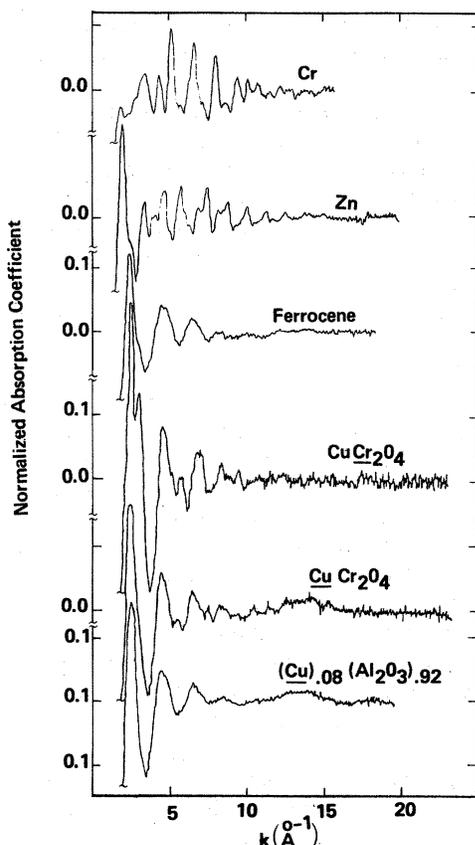
FIG. 8. EXAFS spectra for bcc Cr, hexagonal Zn, ferrocene, Cr, and Cu in $CuCr_2O_4$, an example where two different elements in a compound have different environments and produce different EXAFS, and 8-wt% Cu on Al_2O_3.

hexagonal structure but deviates from perfect hexagonal packing. In ferrocene, the Fe atom is sandwiched between two planar 5-carbon rings so that Fe-C is 2.04 Å, [23] and is shown here as an example of an organometallic compound. The absorption edges of both Cr and Cu in $CuCr_2O_4$ are shown. Both atoms have a distorted octahedral coordination by O. The 8-wt% Cu on Al_2O_3 catalyst sample was found to have a mixture of octahedral and tetrahedral coordination. [5] The two patterns of $CuCr_2O_4$ and $(Cu)_{0.08}(Al_2O_3)_{0.92}$ also show a very long-range EXAFS with a period of approximately 5 Å^{-1}. When Fourier transformed, [5] a peak is found at < 1 Å and may be evidence of scattering from valence electrons in the chemical bond.

V. GRAPHICAL DETERMINATION OF NEAREST-NEIGHBOR DISTANCE

As shown in III, Fourier inversion of EXAFS data is a general and powerful technique to determine many physical parameters; however, it is possible to determine nearest-neighbor distances and phase shifts from a simple graphical technique.

This is possible because the first shell scattering usually dominates the EXAFS curve; then, if only the major EXAFS peaks are used, the period will be that of the first coordination shell. This is illustrated in the following, using the ferrocene spectrum which exhibits primarily a single-shell contribution from the 10 carbon atoms which sandwich the Fe.

The analysis depends on the argument of the sine in Eq. (3):

$$\sin[2kR_j + 2\delta_j(k)] . \tag{11}$$

If δ_j is linear in k,

$$\delta_j = -\alpha_j k + \beta_j . \tag{12}$$

Substituting into the argument of the sine and rearranging, for the first coordination shell, it is convenient to define an n by

$$\tfrac{1}{2}n\pi = 2k(R_1 - \alpha_1) + 2\beta_1 , \tag{13}$$

where $n = 0, 2, 4, \ldots$ for maxima, $n = 1, 3, 5, \ldots$ for minima. A plot of n vs k for the maxima and minima of the measured EXAFS function will determine $R_1 - \alpha_1$ from the slope. Once α_1 is evaluated for a standard, R_1 for unknown materials may be determined. This was done in Fig. 9 for ferrocene and $R_1 - \alpha_1 = 1.61$ Å. Thus $\alpha_1 = 2.045 - 1.61 = 0.44$ Å for Fe in ferrocene. A similar analysis for the metallic Fe EXAFS in Fig. 8 gave $\alpha_1 = 0.40$ Å. This is a typical result for the variation in α with change in chemical bonding.

VI. DISCUSSION

The technique and results shown here describe the practice of EXAFS spectroscopy which can be accomplished with conventional x-ray equipment.
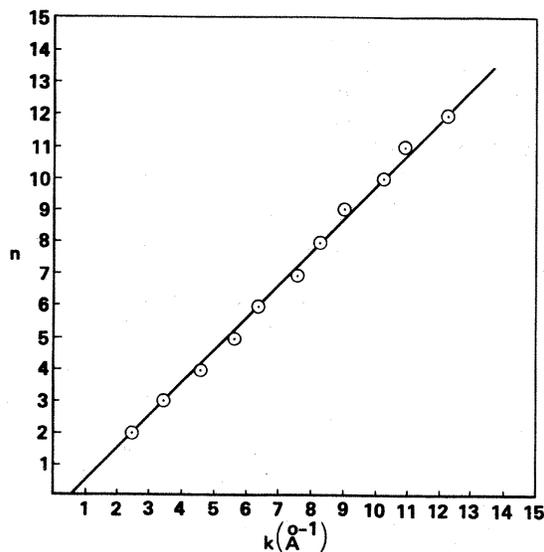
FIG. 9. Graph of n vs k for ferrocene.

The recent success of the EXAFS experiment at the Stanford Synchrotron Radiation Project[24] achieved an order of magnitude improvement in signal to noise ratio and a factor of 3 in resolution; however, the pressure on this facility by potential users is already intense. The improved signal to noise allows more precise EXAFS in a shorter time and the high resolution will allow measurement of the detailed structure in and near the edge; however, the natural width (~ 20 eV) of the EXAFS peaks away from the edge negates the requirement for this additional resolution to measure them. Although one can wish for the easy accessibility of such x-ray sources, for the immediate future most long-term interests in EXAFS spectroscopy must be satisfied with a more conventional experiment such as that shown here.

The experimental practice of using the emission lines present in the incident x-ray spectrum as an energy calibration is satisfactory, and the level of precision achieved in the energy measurement is comparable to the accuracy to which the lines have been measured and tabulated.[17] The largest uncertainty in the E or k scale derives from the inability to measure or calculate the inner potential E_0 (discussed in III).

X-ray counting systems must be fast or corrections for coincident losses are necessary. EXAFS obtained at 77 °K shows much more amplitude and resolution, especially at high k, than that at room temperature. Routine measurements can be made at low temperature. Since the experiments are intensity limited by the x-ray tube, the monochromator must be made as efficient as possible without sacrificing the necessary resolution. LiF is a nearly universal crystal which can be tailored to the required resolution with good (40%) diffraction efficiency.

The data normalization procedure removes the absorption from all other components in the sample, separates the EXAFS from the smoothly varying components, and divides the smoothly varying component into the EXAFS function in preparation for Fourier transformation. If it is desired to compare quantitative results, some such procedure to scale the EXAFS to a per-atom basis is necessary.

The experimental-data section presents normalized data from a variety of pure metals, semiconductors, inorganic and organometallic compounds, and dilute transition metal catalysts on Al_2O_3 supports. Qualitative examination of the data shows the effects of temperature, increasing first-neighbor coordination, atomic structure, and the complexity and variability of the electron-scattering-mean-free-path–temperature envelope in the EXAFS spectrum. The sensitivity of this envelope to type of near neighbor and type of chemical bond may prove to be an additional useful tool for studying the short-range physical properties of materials.

Finally, a simple graphical technique based on the argument of the sine scattering term was used to evaluate the first-neighbor distance from the measured maxima and minima of the EXAFS function, and is presented not as an alternative to the Fourier transformation discussed in III which is so rich in information, but as a simple route to one bit of useful information for someone without a Fourier transformation program.

*Research supported by the National Science Foundation.

[1]E. A. Stern, D. E. Sayers, and F. W. Lytle, following paper, Phys. Rev. B 11, 4836 (1975).

[2]E. A. Stern, Phys. Rev. B 10, 3027 (1974).

[3]D. E. Sayers, E. A. Stern, and F. W. Lytle, Phys. Rev. Lett. 27, 1204 (1971).

[4]D. E. Sayers, F. W. Lytle, and E. A. Stern, J. Non-Cryst. Solids 8-10, 401 (1972).

[5]F. W. Lytle, D. E. Sayers, and E. B. Moore, Appl. Phys. Lett. 24, 45 (1974).

[6]A. E. Sandstrom, in Handbuch der Physik (Springer, Berlin, 1957), Vol. 30, p. 78.

[7]D. E. Sayers, F. W. Lytle, and E. A. Stern. Adv. X-ray Anal. 13, 248 (1970).

[8]H. P. Klug and L. E. Alexander, X-ray Diffraction Procedures (Wiley, New York, 1954), p. 235.

[9]L. G. Parratt, Rev. Mod. Phys. 31, 616 (1959).

[10]R. W. James, The Optical Principles of the Diffraction of X-rays (Bell, London, 1958), p. 268.

[11]J. Vierling, J. V. Gilfrich, and L. S. Birks, Appl. Spectros. 23, 342 (1969); F. W. Lytle, Science 165, 416 (1969).

[12]J. J. Gilman and R. Johnston, Dislocations and Mechanical Properties of Crystals (Wiley, New York, 1957), p. 119.

[13]J. D. Hanawalt, Z. Phys. 70, 293 (1931); J. Franklin Inst. 214, 569 (1932); F. W. Lytle, in Developments in Applied Spectroscopy (Plenum, New York, 1963), p. 285.

[14]V. V. Shmidt, Bull. Acad. Sci. USSR 25, 988 (1961); ibid. 27, 392 (1963).

[15]M. A. Short, Rev. Sci. Instrum. 31, 618 (1960).

[16]R. D. Burbank, Rev. Sci. Instrum. 32, 368 (1961), and cited in H. P. Klug and L. E. Alexander, X-ray Diffraction Procedures for Polycrystalline and Amorphous Materials, 2nd ed. (Wiley, New York, 1974), p. 338.

[17]J. A. Bearden, Rev. Mod. Phys. 39, 78 (1967); J. A. Bearden and A. F. Burr, Rev. Mod. Phys. 39, 125 (1967).

[18]E. R. Cohen and B. N. Taylor, J. Phys. Chem. Ref. Data 2, 663 (1973).

[19]International Tables for X-ray Crystallography III, edited by K. Lonsdale et al. (Kynoch, Birmingham, England, 1962), Sec. 3.2.

[20]W. H. McMaster *et al.*, Report No. UCRL-50174, 1969 (unpublished).

[21]N. K. Del Grande, in *Proceedings of the International Symposium on X-ray Spectroscopy and Electronic Structure of Matter* 1, edited by A. Faessler (University of Munich Press, Munich, 1973), p. 183.

[22]R. A. Van Nordstrand in *Handbook of X-rays*, edited by E. F. Kaelble (McGraw-Hill, New York, 1967), p. 43-1.

[23]A. F. Wells, *Structural Inorganic Chemistry*, 3rd ed. (Oxford, London, 1962), p. 752.

[24]Phys. Today **27**, 17 (1974).